

Solution X-ray scattering (S/WAXS) and structure formation in protein dynamics

Alexandr Nasedkin,^{1,*} Jan Davidsson,^{2,†} Antti J. Niemi^{1,3,4,5,6,7,‡} and Xubiao Peng^{8,§}

¹*Department of Physics, Chalmers University of Technology, SE-412 96 Gothenburg, Sweden*

²*Department of Chemistry, Uppsala University, P.O. Box 803, S-75108, Uppsala, Sweden*

³*Nordita, Stockholm University, Roslagstullsbacken 23, SE-106 91 Stockholm, Sweden*

⁴*Department of Physics and Astronomy, Uppsala University, P.O. Box 803, S-75108, Uppsala, Sweden*

⁵*Laboratoire de Mathématiques et Physique Théorique CNRS UMR 6083,*

Fédération Denis Poisson, Université de Tours, Parc de Grandmont, F37200, Tours, France

⁶*School of Physics, Beijing Institute of Technology, Beijing 100081, P.R. China*

⁷*Laboratory of Physics of Living Matter, School of Biomedicine,*

Far Eastern Federal University, Vladivostok, Russia[¶]

⁸*Department of Physics and Astronomy, University of British Columbia,
Vancouver, British Columbia V6T1Z4, Canada*

We propose to develop mean field theory in combination with Glauber algorithm, to model and interpret protein dynamics and structure formation in small to wide angle x-ray scattering (S/WAXS) experiments. We develop the methodology by analysing the Engrailed homeodomain protein as an example. We demonstrate how to interpret S/WAXS data qualitatively, with a good precision, and over an extended temperature range. We explain experimentally observed phenomena in terms of protein phase structure, and we make predictions for future experiments how to address the data at different ambient temperature values. We conclude that a combination of mean field theory with Glauber algorithm has the potential to develop into a highly accurate, computationally effective and predictive tool for analysing S/WAXS data. Finally, we compare our results with those obtained previously in an all-atom molecular dynamics simulation.

INTRODUCTION

The ability to reduce physical phenomena into simple fundamental laws does not ensure the ability to reconstruct complex physical phenomena from these laws [1]. An atomic level reconstruction often encounters difficulties in large scale systems, and in particular when structural self-organisation takes place. In such scenarios various mean field theoretical descriptions, which build on considerations of symmetry and its breaking in a physical system, can provide a pragmatic alternative [2]. Protein folding and dynamics is an example of a scenario, where the predictions of different approaches can be contrasted against each other. It is a setting where methods of mean field theory and the computationally highly demanding all-atom approach [3, 4] can be compared, and possibly even employed conjointly.

A mean field theory is most effective when the underlying physical system possess symmetries that have become broken. Indeed, various classification schemes [5, 6] of crystallographic Protein Data Bank (PDB) structures reveal that folded proteins are built in an apparently symmetric, modular fashion. A symmetry principle based mean field approach has been introduced, that identifies and models the individual building blocks of a protein in terms of soliton solutions of a generalised discrete nonlinear Schrödinger (DNLS) equation [7, 8]. The DNLS Hamiltonian is the paradigm integrable model [9], its soliton solution has found numerous physical applications [10]. Subsequently it has been proposed that a combination of the ensuing generalised DNLS free energy with fluctuations accounted for using Glauber's descrip-

tion of nonequilibrium statistical mechanics [11–13] can provide both an accurate and a computationally effective way to model protein dynamics. At the same time, all-atom molecular dynamics (MD) simulations are reaching the maturity to describe the folding process of very fast-folding proteins [14]. It has been shown that an analysis of MD folding trajectory in terms of DNLS soliton and concepts of mean field theory provides a highly precise qualitative description how protein folding and dynamics evolves during an all-atom simulation [15].

Here we combine mean field theory including fluctuations computed by Glauber algorithm, to model protein dynamics in the context of small and wide angle solution X-ray scattering (S/WAXS) experiments. S/WAXS is an experimental technique that is emerging as a key tool to study proteins at low resolution [16–19]. We propose that data obtained in a S/WAXS experiment can be simulated and interpreted in a mean field based approach efficiently, with good precision, and over an extended temperature range. For this we consider as an example the *Drosophila melanogaster* Engrailed homeodomain (EnHD). Engrailed is a 61 residue fast-folding two-state protein. It folds via a helical intermediate, and forms a three helix bundle in the folded state. Our reference structure has PDB code 2JWT [20]. This is a NMR structure, and we use the first entry in PDB in our analysis.

Previously the experimental S/WAXS results [21], on which we base our investigation, have been studied using all-atom molecular dynamics (MD) simulations [21]. The Gromacs package [22] and Amber99SB-ILDN force field [23] were employed, over an extended temperature

range.

We compare the results with mean field theoretical simulations in combination with finite temperature Glauber algorithm. We consider a temperature range that covers and extends beyond the available experimental S/WAXS data. We find that a mean field simulation yields a very good description of the experimental observations, and we make predictions for future experiments. A mean field theory based approach significantly reduces the number of degrees of freedom in comparison to an all-atom description, and as a consequence it proceeds several orders of magnitude faster: The results presented here are obtained in a couple of hours *in silico* with a laptop computer.

METHODS

Mean field approach to proteins

Our mean field approach is based on a Landau free energy [2] that relates to the $C\alpha$ backbone geometry. The time scale for a covalent bond oscillation is around 10 ps, thus over biologically relevant time scales the distance between two neighboring $C\alpha$ atoms can be approximated by the time averaged value 3.8 Å. Accordingly, the skeletal $C\alpha$ bond κ and torsion τ angles form a complete set of structural order parameters, to be employed in the construction of a $C\alpha$ trace based Landau free energy [24]. The bond angles are known to be relatively rigid and slowly varying, the differences $\Delta\kappa_i = \kappa_{i+1} - \kappa_i$ between neighboring residues are small. Thus the free energy $E(\kappa, \tau)$ can be expanded in the powers of the differences $\Delta\kappa_i$. A detailed analysis which builds on extensive symmetry considerations, in particular on the requirement that the functional form of the energy should remain invariant under local frame rotations, shows [7, 8, 25–31] that in the limit of small variations in $\Delta\kappa_i$ the following expansion of the free energy can be used in the case of proteins

$$E(\kappa, \tau) = \sum_{i=1}^{N-1} \Delta\kappa_i^2 + \sum_{i=1}^N \left\{ \lambda (\kappa_i^2 - m^2)^2 + \frac{d}{2} \kappa_i^2 \tau_i^2 - b\kappa_i^2 \tau_i - a\tau_i + \frac{c}{2} \tau_i^2 \right\} + \sum_{i \neq j} V(|\mathbf{x}_i - \mathbf{x}_j|) \quad (1)$$

Here (λ, m, a, b, c, d) are parameters. For a given PDB protein structure the parameters are determined by training the minimum energy configuration of (1) to model the PDB backbone.

We recognise in (1) a deformation of the Hamiltonian that defines the discrete nonlinear Schrödinger (DNLS) equation [7, 8]. The three first terms coincide with a *naïve* discretisation of the continuum nonlinear

Schrödinger equation. The fourth term (b) is the conserved momentum in the DNLS model, the fifth (a) term is the Chern-Simons term, and the sixth (c) term is the Proca mass; see [33–36] for a detailed analysis of these contributions. Finally, the last term (V) includes various long distance two-body interactions such as Coulomb and Lennard-Jones interaction between the residues. In the leading order this contribution can be approximated by a hard ball Pauli repulsion [7, 8, 25–31]; see [32] for more general long range interactions.

We validate (1) qualitatively using Privalov’s criteria: According to [37–39] the folding of a protein should be cooperative, and it should resemble a first order phase transition. Indeed, the DNLS equation supports solitons, and solitons are the paradigm cooperative organisers in physical scenarios. A soliton emerges as a solution to the variational equations of (1), and for this we first eliminate the torsion angles using the equation

$$\tau_i[\kappa] = \frac{a + b\kappa_i^2}{c + d\kappa_i^2} \quad (2)$$

For bond angles we then obtain

$$\kappa_{i+1} = 2\kappa_i - \kappa_{i-1} + \frac{dV[\kappa]}{d\kappa_i^2} \quad (3)$$

where

$$V[\kappa] = - \left(\frac{bc - ad}{d} \right) \frac{1}{c + d\kappa^2} - \left(\frac{b^2 + 8\lambda m^2}{2b} \right) \kappa^2 + \lambda \kappa^4$$

The difference equation (3) can be solved iteratively [8]. The ensuing torsion angles are computed from (2), and the $C\alpha$ backbone coordinates are obtained by solving the discrete Frenet equation [24, 40]. A soliton solution models a super-secondary protein structure such as a helix-loop-helix motif, and the loop corresponds to the soliton proper [7, 8, 25–31].

In order to reveal a relation between (1) and the structure of a first order phase transition, we note that in the case of a protein the bond angles are rigid and the torsion angles are flexible. In particular, the variations of κ_i along the backbone are small in comparison to changes in τ_i : We may confirm from (2) that a large change in values of τ_i entails a small change in values of κ_i for parameters that are characteristic to protein backbones. Thus, over sufficiently large distance scales we may try and proceed self-consistently, using only the mean values of the variables. For this we first solve for the mean value of the bond angles $\kappa_i \sim \kappa$ in terms of the mean value of torsion angles $\tau_i \sim \tau$. From (1)

$$\frac{\delta E}{\delta \kappa} = 0 \Rightarrow \kappa^2 = m^2 + \frac{b}{2\lambda} \tau - \frac{d}{4\lambda} \tau^2 \quad (4)$$

In those cases that are of interest to us, this equation always has a solution: Both κ and τ are multivalued

angular variables, and for proteins the parameters b and d are small in comparison with m^2 and λ . We substitute the solution into (1). For the energy this gives

$$-\frac{d^2}{16\lambda}\tau^4 + \frac{bd}{4\lambda}\tau^3 - \left(\frac{b^2}{\lambda} - 2dm^2 - 2c\right)\tau^2 + (a + bm^2)\tau \quad (5)$$

This is the canonical form of the Landau - De Gennes free energy for a first order phase transition, introduced originally in the context of liquid crystals [41]. Thus our qualitative validation of (1) is complete, in the sense that we have confirmed that the free energy (1) appears to be in line with the general arguments in [37–39].

In Appendix A we elaborate on relations between the energy function (1) and elastic network models.

Solitons and Engrailed homeodomain

We construct the $C\alpha$ trace of Engrailed homeodomain as a multi-soliton solution of (3), (2). Our reference configuration is the first entry in the NMR structure with PDB code 2JWT. There are seven individual solitons, including one at each of the flexible N and C terminals. The $C\alpha$ root-mean-square (RMS) distance between the 2JTW and our multisoliton is 0.67\AA , when we use the parameter values that are given in Table I. Note that there are in total 63 parameters including the individual soliton centers, while there are 61 amino acids along the backbone: The presence of solitons enables us to combine the geometry of several amino acids into a single soliton profile, which greatly reduces the number of parameters in (1). Since the number of parameters is *much* smaller than the number of $C\alpha$ coordinates, the model has substantial predictive power that can be scrutinised in experimental scenarios.

In Figure 1 we compare the bond and torsion angle spectra in the PDB structure and the multisoliton. In Figure 2 we show the distance between the individual $C\alpha$ atoms in the PDB structure and the multisoliton. In Figure 3 we show the three dimensional interlaced $C\alpha$ traces for the PDB structure and the multisoliton.

Soliton and Glauber algorithm

We study how the present soliton model of Engrailed responds to variations in ambient temperature using the Glauber algorithm [11–13]. We justify the Glauber algorithm with the following line of arguments: In the case of a simple spin chain the Glauber algorithm reproduces Arrhenius law, and the folding of many short protein chains follows Arrhenius law [3]. Since Engrailed is a relatively short two-state fast-folding protein [42], its folding should obey Glauber dynamics with good accuracy.

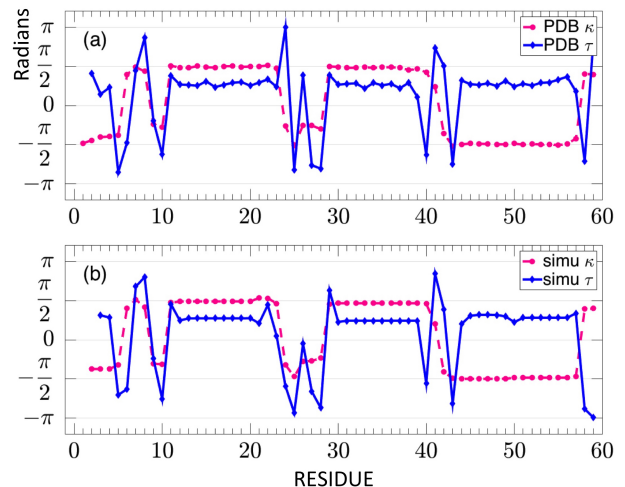


FIG. 1: Color online) (Top) Comparison of bond (κ_i) angles in the first NMR entry of the PDB structure 2JWT and in the ensuing multisoliton solution. (Bottom) Comparison of torsion (τ_i) angles in the first NMR entry of the PDB structure 2JWT and in the ensuing multisoliton solution; note that the torsion angle is defined $\bmod(2\pi)$ thus the apparent differences at sites $i = 24$ and $i = 59$ are smaller than what they appear.

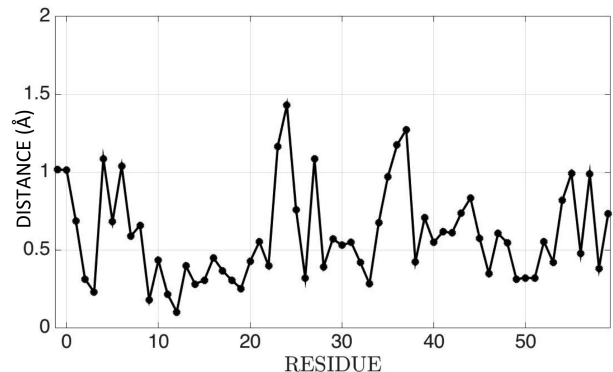


FIG. 2: Color online) The residue-wise distance between the $C\alpha$ atoms in the PDB structure 2JWT (first entry) and the ensuing multisoliton; the grey area corresponds to a 0.2\AA zero point fluctuation distance.

Indeed, Glauber algorithm has a claim to universality in the sense that Glauber dynamics approaches Gibbsian equilibrium distribution at an exponential rate, as expected in a near equilibrium system [11–13].

We perform nine simulations at the Glauber temperature factor values $k\theta = 10^{-12}, 10^{-11}, \dots, 10^{-4}$. Each simulation involves 10^6 Monte Carlo steps and every 1.000^{th} structure is chosen for sampling. We have carefully tested the algorithm length to ensure that we model full thermalisation and for simulation details we refer to [30, 43]. Since the Landau free energy only engages the $C\alpha$ atoms, we employ the *Pulchra* reconstruction program [44] to

soliton	λ_1	λ_2	m_1	m_2	d	c	b
5-6	2.888	1.454	1.174	1.462	1.061 e-09	3.338 e-11	5.953 e-07
8-9	0.664	0.766	1.694	1.565	1.682 e-09	1.667 e-09	2.574 e-07
10-11	6.701	5.39	1.077	1.534	5.441 e-09	1.602 e-09	2.174 e-07
23-24	1.063	0.527	1.682	1.698	0.0	1.234 e-08	1.721 e-07
28-29	7.737	6.699	0.849	1.463	6.187 e-09	1.438 e-09	6.766 e-08
41-42	0.37	0.839	1.674	1.566	0.0	1.009 e-09	3.21 e-08
57-58	7.09	10.196	1.517	1.269	1.962 e-09	9.333 e-09	-2.377 e-07

TABLE I: The parameters in the energy function (1) for 2JWT. The first column defines the center of each soliton, in terms of residue number. For the parameter a we use the fixed value 1.0 e-07, which determines the relative scale between the bond and torsion angle flexibility.

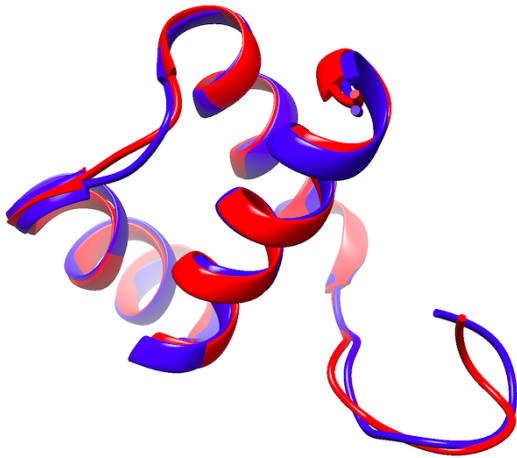


FIG. 3: (Color online) The interlaced $C\alpha$ traces of the PDB structure 2JWT (first entry) (in red) and the ensuing multi-soliton (in blue).

generate the all-atoms structures.

The Glauber temperature factor $k\theta$ does not coincide with the physical temperature T (measured in Kelvin). However, the two can be related by a renormalisation procedure. General arguments presented in [43] suggest that the relation between the two should have the form

$$k\theta = T^\gamma e^{\alpha T - \beta} \quad (6)$$

Unfortunately, the S/WAXS data that is available to us in the case of Engrailed, is not sufficient to determine the parameters in (6). More data is needed, over a more extended temperature range. We hope that future experiments can provide us with such data. Meanwhile, we rely on other experimental techniques to deduce the parameters α , β and γ in (6):

Circular dichroism (CD) spectroscopy can measure the helical content of a protein, as a function of temperature [45]. Accordingly, we can determine the parameters in (6) by comparing the temperature dependence between experimentally observed and simulated helical content. For experimental data we use the CD results on Engrailed that are reported in Figure 3 (bottom) of [46]. For simulation, we first deduce from a statistical analysis of PDB structures that a $C\alpha$ atom which is centered at \mathbf{r}_i can be taken to be in an α -helical position when

$$|\mathbf{r}_{i+4} - \mathbf{r}_i| \approx 6.2 \pm 0.5 \text{ \AA} \quad \& \quad |\tau_i - \tau_0| < 0.6 \text{ (rad)}$$

where τ_0 is the PDB average value of the α -helical torsion angle. In Figure 4 we compare the data that we infer from [46] with $k\theta$ dependence of α -helical content in our Glauber algorithm simulations. From the Figure (4) we deduce the following relation (6),

$$k\theta = T^{0.92} e^{0.113 \times T - 60.9} \quad (7)$$

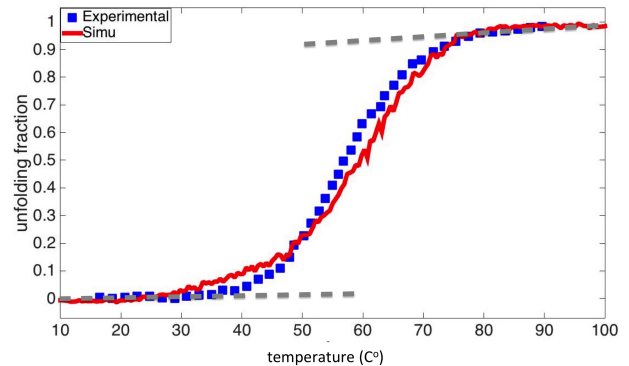


FIG. 4: (Color online) Comparison of simulated temperature dependence in α -helical content with temperature dependence of unfolded fraction observed using 222 nm CD spectra in wild type Engrailed. The experimental data is adapted from Figure 3 (bottom) of [46].

where the physical (experimental) temperature T is measured in Kelvin. For convenience, the conversion between those Glauber temperature factor values that we use in our simulations and Celsius degrees are shown in Table I

In the Figure 4 we also display our estimates for the high temperature and low temperature linear asymptotes. We estimate that there is an onset of linear behaviour above the high (T_h) and below low (T_l) temperature values (order of magnitude)

$$\begin{aligned} T_h &\approx 75 \text{ }^\circ\text{C} \\ T_l &\approx 30 \text{ }^\circ\text{C} \end{aligned} \quad (8)$$

Computations of S/WAXS profiles

We analyse the results from experimental scattering data computations presented in [21]. These computations were performed with CRY SOL software which is part of the ATSAS package [47]. Scattering spectra were calculated in the range of collected S/WAXS spectra, with the solvent density dns set to $340e/nm^3$. The number of spherical harmonics that define the resolution of the scattering curve lm was set to seven. All the other settings of CRY SOL were set to the default values. Scattering spectra were calculated from protein structures containing all the atoms. For details see [21].

Experimental S/WAXS

The scattering patterns that we use were collected at the cSAXS beamline of the Swiss Light Source (SLS) facility at PSI, Switzerland. The EnHD was expressed and purified as previously described in [46]. A moderate concentration of 1.1mM EnHD was dissolved in buffer

$k\theta$	1.0 e-12	1.0 e-11	1.0 e-10	1.0 e-9	1.0 e-8	1.0 e-7	1.0 e-6	1.0 e-5	1.0 e-4
$^{\circ}\text{C}$	~ -25	~ -5	~ 15	~ 35	~ 55	~ 75	~ 95	~ 115	~ 135

TABLE II: Conversion between the simulated Glauber temperature factor values $k\theta$ and the physical temperature values measured in Celsius, obtained using (7).

containing 50 mM HEPES and 100 mM NaCl at pH=8.0. Protein sample was constantly pumped during the experiment allowing fresh sample exposed to the X-rays at all time and thus reducing risk of high-dosage agglomerations. Collected scattering spectra in the range between $q_{min} = 0.07 \text{ \AA}$ and $q_{max} = 0.71 \text{ \AA}$ were used for further analysis; here $q = 4 \sin(\theta / \lambda)$ is the scattering vector, with 2θ the scattering angle of incoming X-rays and λ is the X-ray wavelength.

Scattering pattern at every experimental temperature in [21] is a sample average of separate spectra each of them accumulated during 10 seconds. Datasets were filtered by outlier rejection and tested for possible agglomerations. The experimental error of a scattering curve was calculated as a standard deviation across each dataset.

Optimization algorithm

We fit the simulated S/WAXS spectra to the experimental data in [21]. For this we use the ensemble optimization method [48], it identifies the ensemble of structures which are best representing the experimental spectrum. Fitting is scored based on its χ^2 value indicating a difference between the experimental and theoretical scattering profiles; see for example [49].

We fit each of the theoretically simulated pool to the scattering profiles at every available experimental temperature. We perform optimization runs with 200 iterations, and every iteration returns 10 best-fitted ensembles that we use at the next step. Each ensemble contains a maximum of 20 spectra. We tune mutation and crossing operators for the fastest convergence of the fitting [21]. The code for the optimization algorithm is implemented in a MATLAB package [50].

Comparative all-atom molecular dynamics (MD) simulations

We compare our mean field simulation results with a pool of structures that were obtained in an earlier all-atom molecular dynamics investigation [21]. Those MD simulations were performed using the GROMACS package [22], and the AMBER99SB-ILDN force field [23] with the TIP3P water model [51]; the protein structure was kept at normal pressure, with constant temperature values. Eight MD trajectories were generated for conformational sampling, each trajectory had

a length of 100 ns and sampling was performed every 10 ps. This resulted in 10.000 sampled protein conformations at simulation temperature values $t = 275, 300, 325, 350, 375, 400, 450, 500 \text{ K}$ *i.e.* $t \approx 0, 25, 50, 75, 100, 125, 175$ and $225 \text{ }^{\circ}\text{C}$. Note that these structures were generated *solely* for the purpose of sampling the conformational landscape. Thus the fact that very high and unphysical temperature values were used in some of the simulations is not an issue. In order to compare the simulation results with S/WAXS data, the large number of MD conformers was reduced by clustering them, using structural similarity as a criterion. The central cluster structures were then used as a representative of each cluster, and employed in ensemble fitting with experimental data [21].

RESULTS

We perform comparisons between the mean field model simulations and experimental data, using a number of different criteria:

Radius of gyration

The literature [52–54] commonly attributes three different phases to linearly conjugated polymers; see however [32]: At low temperatures a protein structure is expected to reside in the space filling collapsed phase where attractive forces dominate. At high temperatures where repulsive interactions prevail, a protein structure is in the self-avoiding random walk phase. Between these two phases there is a transition region where the attracting and repelling interactions balance each other, and the protein structure should resemble an ordinary random walk.

The radius of gyration R_g is a widely used order parameter, to determine the phase structure [52–54]. In Figure 5 we show the mean field model distribution of R_g , for each of the nine Glauber temperature factor values that we use in our simulations. In Figure 6 we show the experimentally measured S/WAXS values of R_g , at different temperatures. We note that both in the case of the mean field model and the S/WAXS experiments the R_g distribution has a shape which is reminiscent of a single Gaussian. Moreover, in the case of the mean field model we identify three different regions in Figure 5:

- For the very small temperature factor values $k\theta =$

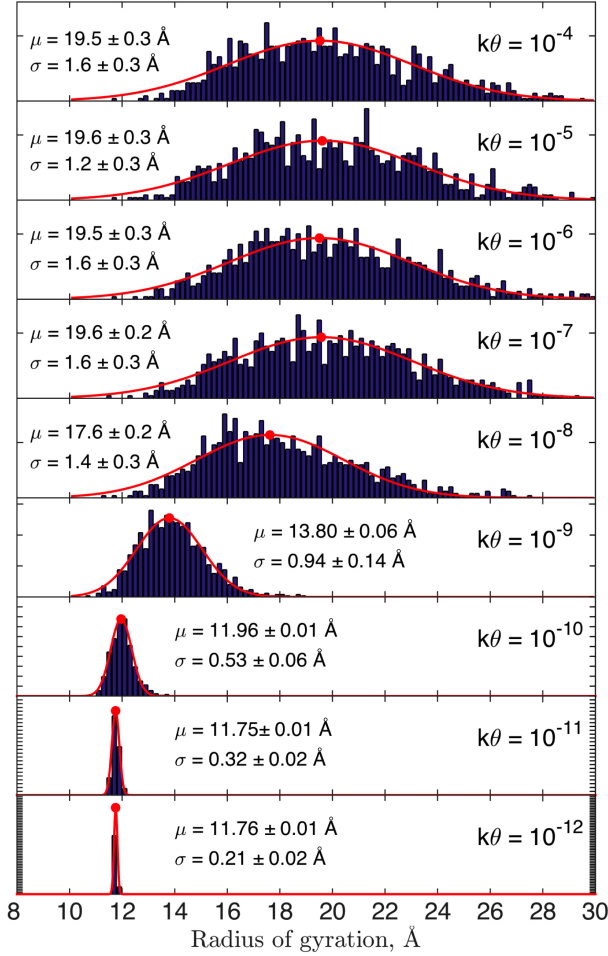


FIG. 5: (Color online) Distribution of the radii of gyration in mean field model simulations at different Glauber temperature factor values.

10^{-12} - 10^{-10} corresponding to physical temperatures below $\sim 15^\circ\text{C}$, the mean value of radius of gyration is stable with value around $\langle R_g \rangle \approx 11.8 - 11.9 \text{ \AA}$. The variance σ is small and increases from $\sigma \sim 0.05 \text{ \AA}$ to $\sigma \sim 0.3 \text{ \AA}$ with increasing $k\theta$.

- The intermediate temperature factor values between 10^{-9} and 10^{-8} covers the physiologically interesting temperature range $\sim 35 - 55^\circ\text{C}$ and constitutes a transition region where the mean value of R_g increases first to $\langle R_g \rangle \approx 13.8 \text{ \AA}$ at $k\theta = 10^{-9}$ and then to $\langle R_g \rangle \approx 17.6 \text{ \AA}$ at $k\theta = 10^{-8}$. The variance increases similarly, first to $\sigma \approx 0.9 \text{ \AA}$ and then to $\sigma \approx 1.9 \text{ \AA}$.

- Finally, when $k\theta = 10^{-7}$ and above corresponding to physical temperature values above $\sim 75^\circ\text{C}$, the distribution becomes stabilised with mean value $\langle R_g \rangle \approx 19.6 \text{ \AA}$ as the variance converges towards the high temperature limit $\sigma \approx 2.5 \text{ \AA}$.

Apparently, the temperature factor values $k\theta = 10^{-12} - 10^{-10}$ correspond to the low temperature col-

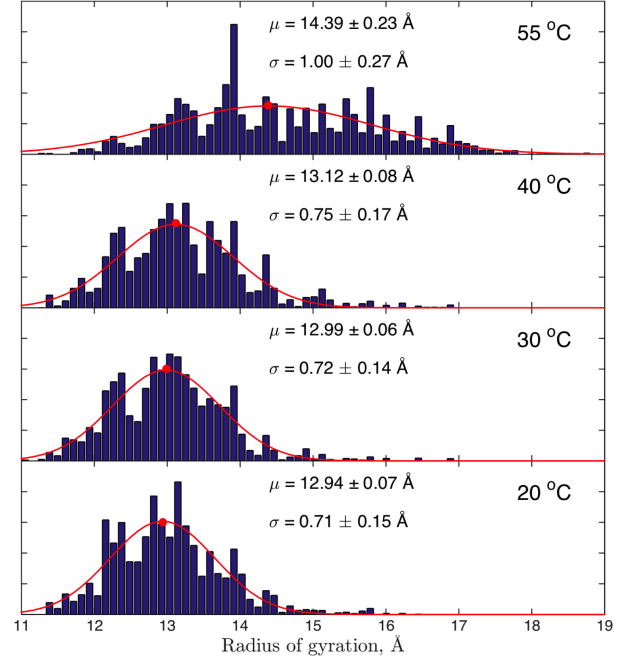


FIG. 6: (Color online) Distribution of the radii of gyration, as recovered from the experimental S/WAXS data at different temperatures.

lapsed phase. The values $k\theta = 10^{-7} \sim 75^\circ\text{C}$ and above correspond to the high temperature self-avoiding random walk phase. Values in the range $10^{-9} - 10^{-8} \sim 35 - 55^\circ\text{C}$ are in the intermediate random walk transition region. See also the experimentally measured CD spectrum [46], shown in Figure 4.

In the experimental S/WAXS data shown in Figure 6 we identify two different regimes:

- When T is in the range $20^\circ\text{C} - 30^\circ\text{C}$ the value of R_g has a very small temperature dependence, with mean $\langle R_g \rangle \approx 12.9 - 13.0 \text{ \AA}$ and variance that is similarly essentially temperature independent with $\sigma \approx 0.5 \text{ \AA}$.
- Between $40^\circ\text{C} - 55^\circ\text{C}$ there is an onset of a transition: Both R_g and σ start increasing so that when $T = 55^\circ\text{C}$ we have $\langle R_g \rangle \approx 14.4 \text{ \AA}$ and $\sigma \approx 1.0 \text{ \AA}$.

Figure 7 shows a comparison between the mean field model results and the experimental S/WAXS data. We observe that the $T = 55^\circ\text{C}$ experimental S/WAXS structures start approaching the self-avoiding random walk phase. Apparently, the fully developed self-avoiding random walk phase is not visible in the temperature range which is covered by the S/WAXS data available to us, according to mean field model. See also Figure 4.

Finally, in Figure 8 we show the R_g values from the MD simulation, adapted from [21]. We observe the following:

- The results up to $T \sim 400\text{K} \sim 125^\circ\text{C}$ are very similar

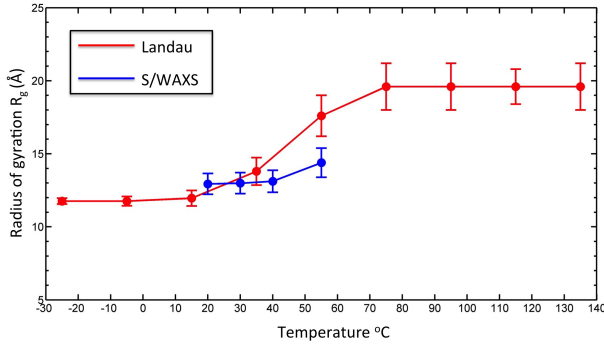


FIG. 7: (Color online) Comparison between the temperature dependence of radius of gyration in the mean field model and in the S/WAXS data. The error-bars denote the one σ of the Gaussian fits, in Figures 5 and 6 respectively.

to the collapsed phase low temperature mean field model results. In particular the $T = 325\text{K}$ and $T = 350\text{K}$ results are very similar to the $k\theta = 10^{-10}$ mean field model results, at the level of the Gaussian distributions.

- Between $T = 400\text{K}$ and $T = 450\text{K}$ there is an apparent transition, and both in the $T = 450\text{K}$ and in the $T = 500\text{K}$ data profiles we identify a mixture of two Gaussian distributions: There is one Gaussian peaked at $T = 450\text{K}$ which is akin the one at collapsed phase in the mean field model. There is one Gaussian peaked at $T = 500\text{K}$ which is akin the experimentally observed low temperature $T = 290\text{K}$ and 310K distributions in the mean field model. There is second Gaussian peaked at $T = 450\text{K}$ which resembles the $k\theta = 310\text{K}$ mean field model distribution. There is also a second Gaussian peaked at $T = 500\text{K}$ which is quite close to the $T = 55^\circ\text{C}$ experimental distribution.

We propose that the double Gaussian distributions that we identify at $T = 450\text{K}$ and $T = 500\text{K}$, reflect the *enormous* computational complexity of MD simulations: The initial configuration that is used in the MD simulations is the experimental reference structure with PDB code 2JWT. Apparently, the available computational resources are not quite sufficient to observe the development of a fully thermalised single Gaussian distribution, akin those we find in the mean field model simulations and the S/WAXS experiment.

We note that the transition in MD simulations between $T = 400\text{K}$ and $T = 450\text{K}$ is in line with [14] where the value $T_c = 390 \pm 7\text{K}$ is reported for the melting temperature of Engrailed homeodomain protein.

Goodness-of-fit analysis

The radius of gyration analysis which is summarised by Figure 7 proposes that the available experimental S/WAXS data in [21] is best described by the mean

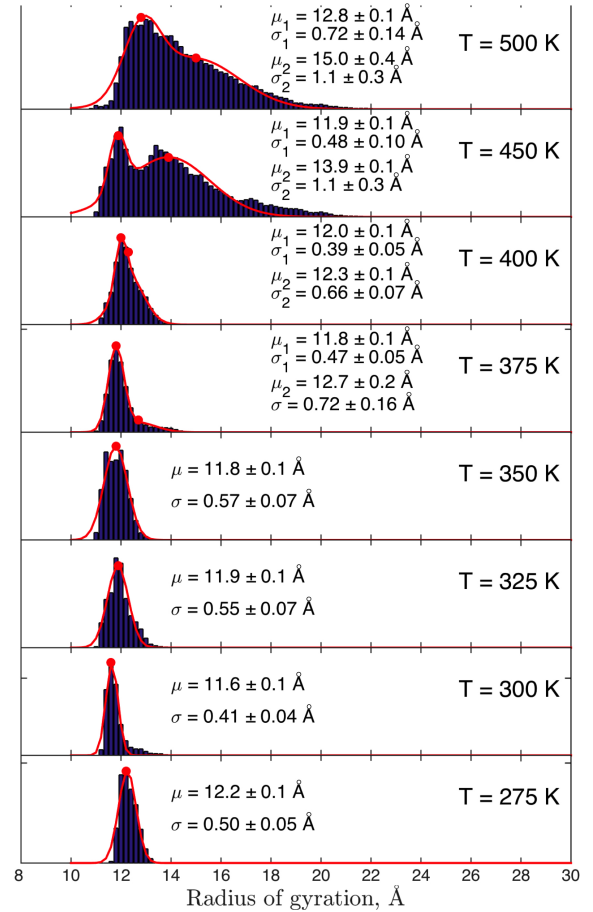


FIG. 8: (Color online) Distribution of the radii of gyration in the MD simulations.

field model when the Glauber temperature factor values are in the range $10^{-10} - 10^{-9}$ *i.e.* $\sim 15 - 35^\circ\text{C}$. In particular, the physiologically relevant $k\theta = 10^{-9} \sim 35^\circ\text{C}$ simulation appears to have a good fit to experimental data, at this temperature.

In Figure 9 we present a *goodness-of-fit* (χ^2) analysis. The Figure displays the χ^2 values we obtain in the mean field model, when we use *Pulchra* [44] to complete the Ca^α backbone into an all-atom model. The result is shown independently for each of the four available experimental S/WAXS temperature value, as a function of the temperature factor $k\theta$.

The results from the χ^2 analysis shown in Figure 9 are in line with the conclusions from the radius of gyration analysis: In the case of mean field model with all-atom *Pulchra* reconstruction, for the $20^\circ\text{C} - 40^\circ\text{C}$ experimental S/WAXS data the minimum value of χ^2 occurs in the vicinity of the mean field model temperature factor value $k\theta = 10^{-9}$. The corresponding χ^2 values are low, in the range $\sim 0.7 - 1.0$. For the highest temperature $T=55^\circ\text{C}$ experimental S/WAXS data, the $k\theta = 10^{-9}$ mean field model simulation with all-atom *Pulchra* yields the numer-

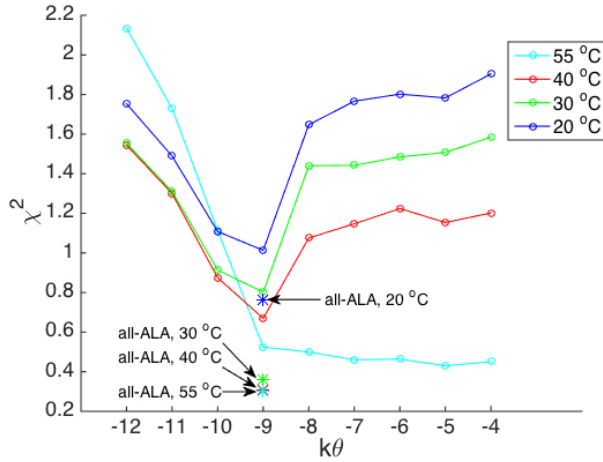


FIG. 9: (Color online) Dependence of the χ^2 values obtained by fitting mean field model simulations, complemented with *Pulchra* all-atom reconstruction. The solid lines connecting circles are a guide for the eye. Also shown separately are χ^2 values we obtain using a simplified $C\alpha$ - $C\beta$ (mock alanine) structure in *Pulchra*.

ical value $\chi^2 = 0.52$. At this temperature the mean field model results with higher $k\theta$ *i.e.* those corresponding to the self-avoiding random walk also produce comparable relatively low χ^2 value, independently of the value of $k\theta$. The reason for this could be in the presence of unusual angles and side-chain orientations in the hydrophobic core of Engrailed [55]. We may expect that with increased temperature, such unusual orientations become washed out by thermal fluctuations, making the *Pulchra* side-chain reconstruction more reliable. We propose this effect is observed in Figure 9, in the χ^2 values at 55 °C

Indeed, it is not clear how reliable an all-atom library such as *Pulchra*, which is designed to model side-chain atoms in static crystallographic protein structures at thermal equilibrium, is in modelling side-chains in a dynamical scenario such as the one considered here. Accordingly we can try and eliminate those effects that are concomitant to the *Pulchra* library. For this we prepare a more rudimental $k\theta = 10^{-9}$ mean field model where we account only for the $C\alpha$ and $C\beta$ atoms. For this we simply replace all side-chains along the Engrailed backbone by (mock) alanine side-chains using *Pulchra*. A comparison between this simplified model and experimental S/WAXS data, for each of the four temperature values, is also shown in the Figure 9; see the individual starred entries. For the more rudimental $C\alpha$ - $C\beta$ (alanine) mean field model the χ^2 values are clearly smaller, than for the all-atom *Pulchra* model; the values are very close to $\chi^2 \approx 0.3$ for the temperature range 30 °C–55 °C. Such a small χ^2 value is *very* close to the background noise limit in the experimental data. Thus a deviation of the simulated data from the experimental data becomes indifferent, at this low level of χ^2 values: At the level of $C\alpha$

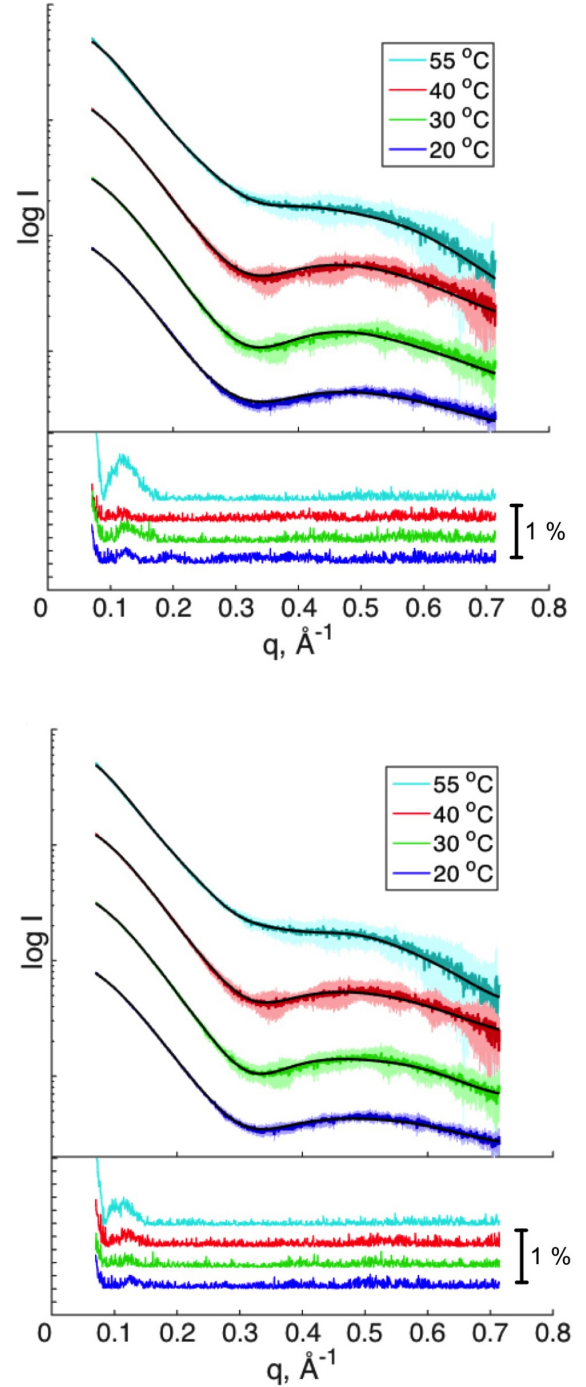


FIG. 10: (Color online) (Top) Fitting of the mean field model pools generated at $k\theta = 10^{-9}$ with the experimental S/WAXS. (Bottom) Same as top, for the mixed temperature MD pool with the experimental S/WAXS. Plots are shifted vertically to enhance visibility. The experimental errors are shown in pale colour. The inset (second plot) in top and bottom Figures shows the difference between experimental and fitted profiles. The inset corresponds to one percent of the scattering intensity extrapolated at $q=0$.

backbone and including the $C\beta$ side chain atoms only,

our simulated results coincide with experimental data, essentially within the error-bars in the latter. Note that when $T = 20^\circ\text{C}$ we obtain the slightly higher $\chi^2 \approx 0.76$ in the case of the $\text{C}\alpha\text{-C}\beta$ backbone, but this is also a clear improvement over the corresponding all-atom *Pulchra* value. See Table III for a summary.

We also estimate the χ^2 values using MD simulations. However, due to limitations in available computer power a fixed-temperature *goodness-of-fit* analysis is not possible. Instead, following [21] we perform an exhaustive fit using a *single* data pool containing *all* the available MD trajectories between 275K and 500K. We then compare this *mixed* pool with the individual experimental data, at the various temperature values. The results are summarised in Table III. We note a clear drop in the values of χ^2 at $T = 55^\circ\text{C}$, when the structures apparently start transiting from the collapsed phase to the self-avoiding random walk phase.

$^\circ\text{C}$	20	30	40	55
χ_{MFM}^2	0.76	0.36	0.31	0.3
χ_{MD}^2	0.72	0.76	0.47	0.31

TABLE III: χ^2 values for the rudimental $\text{C}\alpha\text{-C}\beta$ mean field model (MFM) and MD model. In the case of the mean field model, we use the results with $k\theta = 10^{-9}$ to compare with experimental S/WAXS data. In the case of MD, we combine all available data over the entire temperature range $T = 275 - 500\text{K}$ into a single pool of (statistical) data

In summary, our *goodness-of-fit* analysis shows that at the level of the rudimental $\text{C}\alpha\text{-C}\beta$ (alanine) backbone, the mean field model simulation reproduces the experimental data with very high precision, over an extended temperature range. The simulated results are essentially within the background noise range of the experimental measurements. At the all-atom level the combination of the mean field model with *Pulchra* results in higher χ^2 value. But we note that all-atom reconstruction programs such as *Pulchra* are primarily intended to model static crystallographic protein structures at very low temperatures, not protein dynamics.

S/WAXS scattering curves

In Figure 10 (top) we show how the physiologically relevant mean field model simulation at $k\theta = 10^{-9} \sim 35^\circ\text{C}$ in combination with *Pulchra* all-atom reconstruction, fits the experimentally measured S/WAXS scattering data. We note that the overall quality of the mean field model result is fully comparable to that obtained with the exhaustive MD *mixed* pool fitting [21], shown in Figure 9 (bottom). Besides, the mean field model result is available at individual temperature values and over a wide range of temperatures, which is difficult to achieve in the case of MD using the presently available computa-

tional resources. As in the case of Figure 9 we note that the quality of the mean field model result is presumably hampered by the need to use an all-atom reconstruction procedure such as *Pulchra*, which places the side-chain atoms into their optimal crystallographic (low temperature) thermal equilibrium positions.

CONCLUSIONS

Small to wide angle x-ray scattering (S/WAXS) experiments are emerging as powerful methodology to analyse protein structure and dynamics. As a consequence there is a need to develop computational tools, for structure reconstruction and analysis of S/WAXS data, and for efficient comparison between measurements and theoretical predictions. All-atom molecular dynamics remains the most comprehensive and reliable method to describe the dynamics of a protein, with atomic level scrutiny. However, the enormous demand that it places on of computational power, in particular in a dynamical situation, makes it difficult to productively employ MD in the interpretation of experimental data and structure reconstruction, in solution X-ray scattering experiments. Here we have found that a mean field approach in combination with methods of non-equilibrium statistical mechanics, can provide a pragmatic and computationally highly effective, complementary approach to describe and interpret data in an S/WAXS experiment. Apparently, the mean field model can reach a very good precision over an extended temperature range, with minimal need of computational capacity. We look forward for future S/WAXS experiments that cover a wider temperature range, to compare with our simulation predictions.

ACKNOWLEDGEMENTS

This work was supported by Region Centre Recherche d'Initiative Academique grant, Sino-French Cai Yuanpei Exchange Program (Partenariat Hubert Curien), Vetenskapsrådet, Carl Trygger's Stiftelse för vetenskaplig forskning, and Qian Ren Grant at BIT. The computations were performed on resources provided by the Swedish National Infrastructure for Computing (SNIC) at the High Performance Computing Center North (HPC2N). We thank J. Dai for help in the analysis.

APPENDIX A

Various elastic network models [56–62] have been introduced, to describe aspects of protein dynamics. They have met success in modelling small amplitude oscillations around crystallographic protein structures, in particular the B-factors. Thus it is of interest to investigate

to what extent an elastic network model could be employed to approximate the large scale structural changes that are observed in S/WAXS experiments. In particular, we are motivated to explore connections between (1) and elastic network models.

We simplify our analysis and use the reality, that over a biologically relevant time scale the distance between two neighbouring C α atoms has the value ~ 3.8 Å; the exceptions are *cis*-peptide planes, which are rare. The entire C α backbone can then be reconstructed in terms of its virtual bond and torsion angles (κ_i, τ_i) that appear in (1), using the discrete Frenet equation [40].

We note that the variant of elastic network model considered in [61, 62] employs angular variables $(r_{ab}, \theta_{abc}, \phi_{abcd})$ that relate to the (κ_i, τ_i) in (1). Consequently we base our analysis on the variables in [61, 62]; however, we consider an energy function that has a more general form. The variables in [61, 62] are as follows:

For each C α pair (a, b) that are not nearest neighbour along the backbone, the r_{ab} is their distance. When the structure of peptide planes is fixed, this distance is in effect a function of the bond and torsion angles *i.e.* we have $r_{ab} = r_{ab}(\kappa_i, \tau_i)$ along the C α backbone.

For each triplet $\{a, b, c\}$ of C α atoms, the θ_{abc} is the virtual bond angle; note that $\{a, b, c\}$ do not need to be back-to-back along the C α backbone. These angles are then functions of the C α backbone bond and torsion angles *i.e.* $\theta_{abc} = \theta_{abc}(\kappa_i, \tau_i)$.

For each four consecutive C α atoms $\langle a, b, c, d \rangle$ we have the C α backbone torsion angles ϕ_{abcd} . Thus, these coincide with the torsion angles τ_i in (1).

Note that the set $(r_{ab}, \theta_{abc}, \phi_{abcd})$ is over-complete for the C α backbone, in general there are many more variables than there are C α coordinates (κ_i, τ_i) . For the thermodynamical minimum energy conformation these variables have the values

$$\xi_\alpha \sim (r_{ab}, \theta_{abc}, \phi_{abcd}) \longrightarrow (\hat{r}_{ab}, \hat{\theta}_{abc}, \hat{\phi}_{abcd}) \sim \hat{\xi}_\alpha$$

where we introduce ξ_α as a collective of the $(r_{ab}, \theta_{abc}, \phi_{abcd})$. We are interested in the relevant free energy F around its minimum value. We denote the ensuing deviations in the variables by

$$\begin{aligned} \delta r_{ab} &= r_{ab} - \hat{r}_{ab} \\ \delta \theta_{abc} &= \theta_{abc} - \hat{\theta}_{abc} \\ \delta \phi_{abcd} &= \phi_{abcd} - \hat{\phi}_{abcd} \equiv \tau_i - \hat{\tau}_i \end{aligned} \quad (9)$$

Collectively,

$$\delta \xi_\alpha = \xi_\alpha - \hat{\xi}_\alpha$$

The Taylor expansion of the free energy around the minimum starts with

$$F[r_{ab}, \theta_{abc}, \phi_{abcd}] \equiv F[\xi] = F[\hat{\xi}] +$$

$$+ \sum_\alpha \frac{\partial F}{\partial \xi_\alpha} \delta \xi_\alpha + \frac{1}{2} \sum_{\alpha\beta} \frac{\partial^2 F}{\partial \xi_\alpha \partial \xi_\beta} \delta \xi_\alpha \delta \xi_\beta + \mathcal{O}(\delta \xi^3) \quad (10)$$

The first term evaluates the free energy at the minimum. Since $\hat{\xi}_\alpha$ correspond to this minimum the second term should vanish so that we are left with the following leading order correction to the free energy,

$$\delta F(\xi) = F(\xi) - F(\hat{\xi}) = \frac{1}{2} \sum_{\alpha\beta} \frac{\partial^2 F}{\partial \xi_\alpha \partial \xi_\beta} \delta \xi_\alpha \delta \xi_\beta \quad (11)$$

The variables r_{ab} and θ_{abc} have in general a complex dependency on the C α coordinates (κ_i, τ_i) , but implicit in (11) is the assumption that (at least) to the leading order we have

$$\delta r_{ab} \approx \sum_i \frac{\partial r_{ab}}{\partial \kappa_i} \delta \kappa_i + \frac{\partial r_{ab}}{\partial \tau_i} \delta \tau_i + \mathcal{O}(\delta \xi^2)$$

$$\delta \theta_{abc} \approx \sum_i \frac{\partial \theta_{abc}}{\partial \kappa_i} \delta \kappa_i + \frac{\partial \theta_{abc}}{\partial \tau_i} \delta \tau_i + \mathcal{O}(\delta \xi^2)$$

and

$$\delta \phi = \delta \tau$$

since the torsion angles coincide. Thus, we find to the leading order the following generic elastic network model expression of the free energy,

$$\delta F(\kappa, \tau) = \sum_{i,j} \{ \Gamma_{ij}^{\kappa\kappa} \delta \kappa_i \delta \kappa_j + \Gamma_{ij}^{\kappa\tau} \delta \kappa_i \delta \tau_j + \Gamma_{ij}^{\tau\tau} \delta \tau_i \delta \tau_j \} \quad (12)$$

with connectivity matrices $\Gamma^{\kappa\kappa}, \Gamma^{\kappa\tau}, \Gamma^{\tau\tau}$ that are independent of the backbone coordinates (κ_i, τ_i) . Different choices of Γ specify different elastic network models. Commonly, the connectivity matrix is taken to vanish when the spatial distance $|\mathbf{x}_i - \mathbf{x}_j|$ between the C α carbons i and j exceeds a prescribed value. Note that we may also write (12) in terms of the variables (κ, τ) in (1), as follows

$$= \sum_i \{ A_i \kappa_i + B_i \tau_i \} + \sum_{i,j} \{ C_{ij} \kappa_i \kappa_j + D_{ij} \kappa_i \tau_j + E_{ij} \tau_i \tau_j \} \quad (13)$$

with κ, τ independent but in general $|\mathbf{x}_i - \mathbf{x}_j|$ dependent connectivity matrices A, \dots, E .

In the case of (1), the functional form of the energy follows from symmetry considerations [7, 8, 25–31]. In particular, the principle that the energy should remain invariant under local frame rotations is exploited to arrive at the functional form (1). We now inquire whether similar symmetry considerations could be introduced to deduce a nonlinear extension of the energy function (12), (13), in some kind of a natural fashion. For this we start with the following complex valued quantity

$$\mathcal{F}(\Psi) \sim \sum_{ij} \Psi_i^\dagger V_{ij}(|\mathbf{x}_i - \mathbf{x}_j|) \Psi_j \quad (14)$$

where

$$\Psi_i \equiv \Psi(\mathbf{x}_i) = \begin{pmatrix} e^{i\varphi_{12}} \cos \vartheta \\ e^{i\varphi_{34}} \sin \vartheta \end{pmatrix} \quad (15)$$

The free energy of interest is then a linear combination of real and imaginary parts of (14).

We note that (14) engages a structure akin a O(4) spin glass model, in a spinorial representation [33–36].

For a symmetry principle, we demand that (14) should remain invariant under a local U(1) rotation that sends

$$\Psi_i \equiv \Psi(\mathbf{x}_i) \rightarrow e^{i\eta(\mathbf{x}_i)} \Psi(\mathbf{x}_i) \quad (16)$$

We take the connectivity matrix V in (14) to have the form

$$V(|\mathbf{x}_i - \mathbf{x}_j|) = \begin{pmatrix} \rho_{ij}^{11} & \rho_{ij}^{12} \\ \rho_{ij}^{21} & \rho_{ij}^{22} \end{pmatrix} \cdot e^{i \int_{\mathbf{x}_j}^{\mathbf{x}_i} \mathbf{A} \cdot d\mathbf{x}} \quad (17)$$

with $\rho_{ij}^{ab} = \rho^{ab}(|\mathbf{x}_i - \mathbf{x}_j|)$. When we choose the vector field $\mathbf{A}(\mathbf{x})$ to transform according to

$$\mathbf{A}(\mathbf{x}) \rightarrow \mathbf{A}(\mathbf{x}) + \nabla \eta \quad (18)$$

under the U(1) rotation (16), the functional (14) remains intact under the combined transformation (16), (18). For consistency, to ensure that (17) is independent of the path connecting \mathbf{x}_i and \mathbf{x}_j , we demand that [36]

$$\nabla \times \mathbf{A} = 0 \quad \Rightarrow \quad \mathbf{A} = \nabla \Phi \quad (\text{locally})$$

We proceed to identify U(1) invariant combinations of the variables in (15): With $(\sigma_1, \sigma_2, \sigma_3)$ the standard Pauli matrices we define the three component unit vector

$$\hat{\mathbf{n}} = \Psi^\dagger \hat{\sigma} \Psi \Rightarrow \mathbf{n} = \begin{pmatrix} \sin 2\vartheta \cos(\varphi_{34} - \varphi_{12}) \\ \sin 2\vartheta \sin(\varphi_{34} - \varphi_{12}) \\ \cos 2\vartheta \end{pmatrix} \quad (19)$$

Clearly, this vector is invariant under the U(1).

We note that the torsion angle τ in (1) has a natural interpretation as the longitude on a two-sphere, and the bond angle κ has similarly a natural identification as the latitude [7, 8, 25–31]. Thus these variables can be combined into a three component unit vector such as (19), in a canonical fashion. Accordingly we have the U(1) invariant identifications

$$\begin{aligned} \tau &= \varphi_{34} - \varphi_{12} \\ \kappa &= 2\vartheta \end{aligned}$$

The U(1) gauge transformation (16) then corresponds to a frame rotation, around the direction of \mathbf{n} [7, 8, 25–31].

We choose the gauge so that

$$\mathbf{A} = \nabla \left\{ \frac{1}{2}(\varphi_{34} + \varphi_{12}) \right\}$$

and we substitute this in (14). We work out the real and imaginary part of (14) separately, and Taylor expand the trigonometric functions to second order to find

$$\begin{aligned} \text{Re } \mathcal{F}[\kappa, \tau] &= \frac{1}{2} \sum_{i,j} \{ \rho_{ij}^{12} + \rho_{ij}^{21} \} \kappa_j \\ &- \frac{1}{4} \sum_{i,j} \rho_{ij}^{11} \{ (\tau_i - \tau_j)^2 + \kappa_j^2 \} + \frac{1}{4} \sum_{i,j} \rho_{ij}^{22} \kappa_i \kappa_j \end{aligned} \quad (20)$$

$$\text{Im } \mathcal{F}[\kappa, \tau] = \frac{1}{2} \sum_{i,j} \{ \rho_{ij}^{12} - \rho_{ij}^{21} \} (\tau_i + \tau_j) \kappa_j \quad (21)$$

A frame independent energy function akin (13) can then introduced, as a linear combination of (20), (21) and with ρ_{ij}^{ab} the connectivity matrix.

There is a notable conceptual differences between (1), and (13): The free energy (13) is a quadratic function of the variables while (1) is quartic. Thus the soliton that constitutes the hallmark of the DNLS equation and models a protein loop in the approach based on (1), is absent in conventional (linear) elastic network models; the loops have a different origin, in the latter.

Moreover, unlike (1) where only nearest neighbour couplings appear explicitly, in the elastic network models there can be a direct, space coordinate dependent coupling between *any* two amino acids i and j . As a consequence, in an elastic network model the number of parameters is commonly much larger than the number of independent C α coordinates. For example [62] estimates in concrete examples, that the number of independent angular variables in their elastic network model is about 15-17 times larger than the number of independent backbone angles. On the other hand, in the case of (1), the number of parameters is commonly comparable to the number of amino acids which yields much tighter experimental constraints on the model.

The commonly employed linear elastic network models are by their design describing the small amplitude motions around a protein conformation that corresponds to a minimum of free energy, such as a crystallographic protein structure. These models are not even designed to describe the large conformational deformations that one encounters in S/WAXS experiments, in their present form they are not intended to describe large structural deviations from the minimum energy [59, 60].

We conclude that elastic network models have their conceptual foundation in spin glass models [63] while the energy function (1) builds on the concept of collective oscillations and large scale structure formation in conventional nonlinear dynamics. Accordingly, these two approaches are complementary to each other. In a future publication we shall investigate the O(4) spin glass model (14), to systematically account for non-linear corrections in the context of the elastic network model along the lines of the DNLS model.

References

-
- * Electronic address: alexandr.nasedkin@chalmers.se
† Electronic address: jan.davidsson@kemi.uu.se
‡ Electronic address: Antti.Niemi@physics.uu.se
§ Electronic address: xubiaopeng@gmail.com
¶ URL: <http://www.folding-protein.org>
- [1] P. Anderson, Science **177** 393(1972)
 - [2] N. Goldenfeld, *Lectures On Phase Transitions And The Renormalization Group* (Addison-Wesley, 1992)
 - [3] E. Alm, D. Baker, Curr. Opin. Struct. Biol. **9** 189 (1999)
 - [4] D. Baker, Nature **405** 39 (2000)
 - [5] I. Sillitoe, A. L. Cuff, B. H. Dessailly, N. L. Dawson, N. Furnham, D. Lee, J. G. Lees, T. E. Lewis, R. A. Studer, R. Rentzsch, C. Yeats, J. M. Thornton, C. A. Orengo, Nucleic Acids Res **41** D490(2013)
 - [6] A.G. Murzin, S. E. Brenner, T. Hubbard, C. Chothia, J. Mol. Biol. **247** 536 (1995)
 - [7] M. Chernodub, S. Hu, A. J. Niemi, Phys. Rev. **E82** 011916 (2010)
 - [8] N. Molkenhuth, S. Hu, A. J. Niemi, Phys. Rev. Lett. **106** 078102 (2011)
 - [9] L.D. Faddeev, L.A. Takhtajan *Hamiltonian methods in the theory of solitons* (Springer Verlag, Berlin, 1987)
 - [10] P.G. Kevrekidis, *The discrete Nonlinear Schrödinger equation: Mathematical Analysis, Numerical Computations and Physical Perspectives* (Springer Verlag, Berlin, 2009)
 - [11] R.J. Glauber, J. Math. Phys. **4** 294(1963)
 - [12] A.B. Bortz, M. H. Kalos, J. L. Lebowitz, J. Comput. Phys. **17** 10(1975)
 - [13] B.A. Berg, *Markov Chain Monte Carlo Simulations And Their Statistical Analysis* (World Scientific, Singapore, 2014)
 - [14] K. Lindorff-Larsen, S. Piana, R. O. Dror, D. E. Shaw, Science **334** 517(2011)
 - [15] J. Dai, A.J. Niemi, J. He, A. Sieradzan, N. Ilieva, Phys. Rev. **E93** 032409 (2016)
 - [16] S. Doniach, Chem Rev. **101** 1763 (2001)
 - [17] C.D. Putnam, M. Hammel, G. L. Hura, J. A. Tainer, Q. Rev. Biophys. **40** 191(2007)
 - [18] R.P. Rambo, J. A. Tainer, Curr. Opin. Struc. Biol. **20** 128 (2010)
 - [19] C.E. Blanchet, D.I. Svergun, Annu. Rev. Phys. Chem. **64** 37 (2013)
 - [20] T.L. Religa, J. Biomol. NMR **40** 189 (2008)
 - [21] A. Nasedkin, M. Marcellini, T. L. Religa, S. M. Freund, A. Menzel, A. R. Fersht, P. Jemth, D. van der Spoel, J. Davidsson, PLoS ONE **10** e0125662 (2015)
 - [22] S. Pronk, S. Pall, R. Schulz, P. Larsson, P. Bjelkmar, R. Apostolov, M. R. Shirts, J. C. Smith, P. M. Kasson, D. van der Spoel, B. Hess, E. Lindahl, Bioinformatics **29** 845(2013)
 - [23] K. Lindorff-Larsen, S. Piana, K. Palmo, P. Maragakis, J. L. Klepeis, R. O. Dror, D. E. Shaw, Proteins **78** 1950 (2010)
 - [24] K. Hinsén, S. Hu, G.R. Kneller, A.J. Niemi, JCP **139** 124115 (2013)
 - [25] A.J. Niemi, Phys. Rev. **D67** 106004 (2003)
 - [26] U.H. Danielsson, M. Lundgren, A.J. Niemi, Phys. Rev. **E82** 021910 (2010)
 - [27] S. Hu, A. Krokhotin, A. J. Niemi, X. Peng, Phys. Rev. **E83** 041907 (2011)
 - [28] A. Krokhotin, A. Liwo, A.J. Niemi, H.A. Scheraga, J. Chem. Phys. **137** 035101 (2012)
 - [29] A. Krokhotin, M. Lundgren, A.J. Niemi, Phys. Rev. **E86** 021923 (2012)
 - [30] A. Krokhotin, A.J. Niemi, X. Peng, J. Chem. Phys. **138** 175101 (2013)
 - [31] A.J. Niemi, *Gauge field, strings, solitons, anomalies and the speed of life - Lectures at the Les Houches Summer School on Topological methods in condensed matter* (arXiv preprint [arXiv:1406.7468](https://arxiv.org/abs/1406.7468))
 - [32] A. Sinelnikova, A.J. Niemi, M. Ulybyshev, Phys. Rev. **E92** 032602 (2015)
 - [33] S. Hu, Y. Jiang, A.J. Niemi Phys. Rev. **D87** 105011 (2013)
 - [34] T. Ioannidou, Y. Jiang, A.J. Niemi, Phys. Rev. **D90** 025012 (2014)
 - [35] T. Ioannidou, A.J. Niemi Phys. Lett. **A380** 333 (2016)
 - [36] I. Gordeli, D. Melnikov, A.J. Niemi, A. Sedrakyan, Phys. Rev. **D94** 021701 (2016)
 - [37] P.L. Primalov, Adv. Protein Chem. **33** 167 (1979)
 - [38] P.L. Primalov, Ann. Rev. Biophys. Biophys. Chem. **18** 47 (1989)
 - [39] E. Shakhnovich, A. Finkelstein Biopolymers **28** 1667 (1989)
 - [40] S. Hu, M. Lundgren, A.J. Niemi, Phys. Rev. **E83** 061908 (2011)
 - [41] P.G. de Gennes, J. Prost *The Physics of Liquid Crystals* (Clarendon Press, Oxford, 1995)
 - [42] U. Mayor, J.G. Grossmann, N.W. Foster, S.M.V. Freund, A.R. Fersht, J. Mol. Biol. **333** 977 (2003)
 - [43] A. Krokhotin, M. Lundgren, A. J. Niemi, X. Peng, J. Phys. (Cond. Mat.) **25** 325103 (2013)
 - [44] P. Rotkiewicz, J. Skolnick, J. Comput. Chem. **29** 1460(2008)
 - [45] S.M. Kelly, T.J. Jess, N.C. Price, Biochim. Biophys. Acta **1751** 119 (2005)
 - [46] S.E. Ades and R.T. Sauer, Biochemistry **33** 9187 (1994)
 - [47] M.V. Petoukhov, D. Franke, A. V. Shkumatov, G. Tria, A. G. Kikhney, M. Gajda, C. Gorba, H. D. T. Mertens, P. V. Konarev, D. I. Svergun, J. Appl. Crystallogr. **45** 342 (2012)
 - [48] P. Bernado, E. Mylonas, M.V. Petoukhov, M. Blackledge, D.I. Svergun, J. Am. Chem. Soc. **129** 5656 (2007)
 - [49] D. Schneidman-Duhovny, M. Hammel, A. Sali, Nucl. Acids Res. **38** W540 (2010)
 - [50] Package available from the corresponding author upon request.
 - [51] W.L. Jorgensen, J. Chandrasekhar, J.D. Madura, R.W. Impey, M.K. Klein J. Chem. Phys. **79** 926 (1983)
 - [52] P.G. De Gennes *Scaling Concepts in Polymer Physics* (Cornell University Press, Ithaca, 1979)
 - [53] A.Yu. Grosberg, A.R. Khokhlov *Statistical Physics of Macromolecules* (AIP Series in Polymers and Complex Materials, Woodbury, 1994)
 - [54] L. Schäfer, *Excluded Volume Effects in Polymer Solutions, as Explained by the Renormalization Group* (Springer Verlag, Berlin, 1999)
 - [55] W. Banachewicz, T. L. Religa, R. D. Schaeffer, V. Daggett, A. R. Fersht, P. Natl. Acad. Sci. USA **108** 5596(2011)

- [56] I. Bahar, A.R. Atilgan, B. Erman, *Folding and Design* **2** 173 (1997)
- [57] T. Haliloglu, I. Bahar, B. Erman, *Phys. Rev. Lett.* **79** 3090 (1997)
- [58] A.R. Atilgan, S.R. Durell, R.L. Jernigan, M.C. Demirel, O. Keskin, I. Bahar, *Biophys. J.* **80** 505 (2001)
- [59] T.R. Lezon, I.H. Shrivastava, Z. Yang, I. Bahar, in *Handbook on Biological Networks* Edited by S. Boccaletti, V. Latora, Y. Moreno (World Scientific, Singapore, 2010)
- [60] I. Bahar, T.R. Lezon, L.-W. Yang, E. Eyal, *Annu. Rev. Biophys.* **39** 23 (2010)
- [61] A. Srivastava, R.B. Halevi, A. Veksler, R. Granek, *Proteins* **80** 2692 (2012)
- [62] A. Srivastava, R. Granek, *Proteins* **84** 1767 (2016)
- [63] J.D. Bryngelson, P.G. Wolynes, *Proc. Natl. Acad. Sci. USA* **84** 7524 (1987)